Advanced Composites and Hybrid Materials (2020) 3:473–484
https://doi.org/10.1007/s42114-020-00191-z

ORIGINAL RESEARCH

Hyperelastic magnetic reduced graphene oxide three-dimensional framework with superb oil and organic solvent adsorption capability

Yaqing Wang[1] · Wenhao Xie[1] · Hu Liu[2] · Hongbo Gu[1]

Received: 3 October 2020 / Revised: 1 November 2020 / Accepted: 14 November 2020 / Published online: 2 December 2020

Abstract

Three-dimensional (3D) porous network materials with large pore volume, high specific surface area, and controllable porosity have potential application in wastewater treatment. This work aims to develop a novel hyperelastic and ultra-light magnetic reduced graphene oxide (rGO-Fe_3O_4) 3D framework with a density of 4.52 mg cm^{-3} through a covalent bond of aminated nanomagnetite (Fe_3O_4-NH_2) onto graphene oxide (GO) and subsequent reduction. This 3D framework exhibited high adsorption capacities to ethyl acetate (215.8 ± 11.8 g g^{-1}), cyclohexane (239.7 ± 9.9 g g^{-1}), acetone (149.1 ± 6.5 g g^{-1}), dichloromethane (308.0 ± 16.4 g g^{-1}), and sesame oil (204.7 ± 10.2 g g^{-1}), which were much higher than those of pure rGO aerogel (45.6 ± 2.3 g g^{-1} to ethyl acetate). Meanwhile, the 3D framework demonstrated superelastic mechanical properties with a 100% recoverability during the cyclic compression loading tests under an optimal fabrication condition of 1 mg mL^{-1} GO concentration and 3:1 mass ratio of GO to Fe_3O_4-NH_2 nanoparticles. Most importantly, this rGO-Fe_3O_4 3D framework could achieve an effective oil/water separation within only 25 s and maintained an outstanding adsorption capability to ethyl acetate after 10 cycles of the adsorption/desorption process without any obvious change, depicting an excellent recyclability and reusability. This work aims to provide a promising material for environmental control and oil/organic solvent adsorption.

Keywords Graphene 3D framework · Aminated nanomagnetite · Covalent bond · Oil/organic solvent adsorption

1 Introduction

The frequent occurrence of oil spills in the oil exploration and transportation process [1], for example, Amoco Milford Haven oil spill [2] and Gulf of Mexico oil spill [3], has resulted in the waste of energy sources and polluted the marine ecological environment [4, 5]. Oil spill in water can seriously harm human health as well [6]. In addition to oil spills, the discharge of a large amount of industrial oily sewage and organic solvent wastewater further threatens the public health and terrestrial ecosystems [7]. Currently, the main methods to handle oil spill and organic solvent wastes include chemical treatment (such as surfactants), in situ combustion, and bioremediation [8–11]. These methods could alleviate the harm of oil spill and organic solvent wastes to a certain extent, but the high operation cost, secondary contamination, and relatively low treatment efficiency restrict their large-scale deployment [12].

Among these methods, adsorption has the advantages of low cost and high efficiency for removing oil and organic solvent wastes [13]. The materials used in the adsorption process could be roughly divided into four types, i.e., zero-dimensional (0D), one-dimensional (1D), two-dimensional (2D), and three-dimensional (3D) matrix materials. Nevertheless, the recycling of 0D (for example, calcite [14], silica nanoparticles, nickel oxide [15], ferric oxide [16], and other metal oxide) and 1D (including carbon nanotubes [17], cellulose nanofibers [18]) adsorbents is still a challenge. 2D materials, such as electrospun nanofibrous mat [19], cotton fabrics [20, 21], and membrane [22], have very poor oil and organic solvent waste retention capability. Although 3D graphene aerogel has shown good oil adsorption capacity

✉ Hongbo Gu
hongbogu2014@tongji.edu.cn

✉ Hu Liu
liuhu@zzu.edu.cn

[1] Key Lab of Chemical Assessment and Sustainability, School of Chemical Science and Engineering, Tongji University, Shanghai 200092, China

[2] Key Laboratory of Materials Processing and Mold (Zhengzhou University), Ministry of Education, National Engineering Research Center for Advanced Polymer Processing Technology, Zhengzhou University, Zhengzhou, China

[23], the lack of elasticity and the difficulty of recycling limit its practical applications. To solve the recycling problem, magnetic nanoparticles are usually loaded onto graphene aerogel, which realize the rapid separation of graphene aerogels after adsorption under the applied external magnetic field [24, 25].

The attachment of magnetic nanoparticles onto graphene could be achieved via two ways: covalent bond and physical adsorption [26]. Usually, physical adsorption driven by the van der Waals force has the problem of weak interactions and the nanoparticles are easily detached upon the exposure to harsh environments. As for the covalent bond method, organic compounds or functional polymers (mostly organic molecular chains) are commonly adopted as bonding media or bridge. The surface of magnetic nanoparticles is functionalized by appropriate organic compounds, and a hybrid assembly is possible to be formed [27]. Because of the covalent bond, magnetic nanoparticles could be evenly distributed on the surface of graphene. Meanwhile, the formation of aggregates is avoided and a quantitative loading is able to be attained through the control of functional groups. To date, the graphene aerogels covalently bonded with uniformly distributed magnetic nanoparticles have not been reported for oil and organic solvent adsorption yet.

In this study, stable magnetic graphene aerogels (rGO-Fe_3O_4) have been constructed via covalently bonded aminated nanomagentite (Fe_3O_4-NH_2) onto graphene oxide and subsequent reduction process. The covalent bond between amine group on nanomagentite and carboxyl group on graphene oxide helps nanomagentite to be uniformly distributed on the graphene sheets, and the subsequent reduction process (i.e., high-temperature annealing) makes the final rGO-Fe_3O_4 aerogels more hydrophobic which favors the adsorption of oil and organic solvents. The fabrication conditions for the rGO-Fe_3O_4 3D framework have been exploited to acquire the optimal structure, excellent adsorption performance, and recyclability by considering the concentrations of the GO solution and weight ratio of GO to Fe_3O_4-NH_2. The magnetic rGO-Fe_3O_4 aerogels exhibit a strong mechanical property and hyperelasticity. Compared with pure rGO aerogel, this superelastic rGO-Fe_3O_4 3D framework displays an outstanding adsorption capacity, high oil/water separation efficiency, superb recyclability and reusability.

2 Experimental

2.1 Materials

Graphite sheets (325 meshes, 99.5%) were provided by Alpha Essar Co., Ltd. (Shanghai, China). Triethylenetetramine (> 98%) was purchased from TCI-Tixi Ai (Shanghai) Chemical Industry Development Co., Ltd. Potassium persulfate (99.0%) was obtained from Beijing InnoChem Science & Technology Co., Ltd. Acrylic acid (> 99.7%), phosphorus pentoxide (98.0%), *L*-ascorbic acid (> 99.7%), hexane (> 99.5%), acetone (> 99.5%), ethyl acetate (> 99.5%), concentrated sulfuric acid (95.0–98.0 wt%), hydrogen peroxide (30 wt%), ammonium persulfate (≥ 98.5%), and potassium permanganate (99.5%) were supplied by Sinopharm Chemical Reagents Co., Ltd. Fe_3O_4 nanoparticles were obtained from Nanjing Emperor Nano Material Co., Ltd. Dichloromethane (> 99.5%) was offered by Aladdin Reagent (Shanghai) Co., Ltd. All chemicals were used as-received without any pretreatment.

2.2 Preparation of magnetic reduced graphene oxide aerogels

Graphene oxide (GO) was prepared by a modified Hummers method [28]. Briefly, graphite powder was pre-oxidized by potassium persulfate and phosphorus pentoxide in concentrated sulfuric acid at 80 °C under magnetic stirring. After being washed with deionized water to neutral, the products were dissolved in concentrated sulfuric acid together with potassium permanganate under mechanical stirring in ice-water bath. Then, the reaction was continued with raising temperature to 35 °C for mechanical stirring of 2 h. Finally, the GO was obtained with adding deionized water and 30 wt% of hydrogen peroxide. Aminated magnetite nanoparticles (Fe_3O_4-NH_2) were made by functionalizing Fe_3O_4 nanoparticles with amino groups following the reported procedures [29]. In short, the Fe_3O_4 nanoparticles and ammonium persulfate were put in deionized water at 70 °C. Then, acrylic acid was dripped into the solution for reaction of 4 h. Thereafter, triethylenetetramine droplets were added into the above solution for amination reaction of 3–4 h to acquire Fe_3O_4-NH_2. The detailed preparation process of GO and Fe_3O_4-NH_2 are listed in supplementary materials. After that, Fe_3O_4-NH_2 were sonicated in 30 mL deionized water and added into 3 mg mL^{-1} of GO solution with a mass ratio of GO to Fe_3O_4-NH_2 of 3: 1 under a mechanical stirring at 70 °C for 2 h, and then cooled down to room temperature. This process ensured the formation of the covalent bond between Fe_3O_4-NH_2 and GO, which was also confirmed in the literature [30]. After that, *L*-ascorbic acid with a mass ratio to GO of 2:1 was introduced into the above solution and sonicated for 10 min. (*L*-Ascorbic acid, known as *Vitamin C*, a common antioxidant in the cells, has two active hydroxyl groups on the double bond of a five-membered ring in its molecular structure. *L*-Ascorbic acid can be easily dissociated with two protons to form the oxygen anions, which are able to replace the hydroxyl and epoxide groups in GO. Consequently, GO was reduced by the subsequent elimination reaction and dehydroascorbic acid was further decomposed into other oxidation products [31].) Then, the mixture was sealed and maintained in a regular oven at 70 °C for 4 h to attain the magnetic graphene oxide hydrogel.

The hydrogel was dialyzed in 15 *v*/v% aqueous alcohol solution for about 6 h. After freezing in the refrigerator for 18 h, the frozen hydrogel was put into the freeze-dryer for 48 h to fabricate the magnetic rGO-Fe_3O_4 aerogel. Finally, this magnetic aerogel was placed in an infrared tube furnace (Beijing Huace Testing Instrument Co., Ltd.) under a nitrogen atmosphere and annealed at 450 °C for 1 h to acquire the superelastic magnetic reduced graphene oxide (rGO-Fe_3O_4) 3D framework. The preparation process is shown in Fig. 1. Different mass ratios of GO to Fe_3O_4-NH_2 including 4:1, 2:1, and 1:1 and different GO concentrations such as 0.5, 1, 2, 4, and 5 mg mL^{-1} were also applied to synthesize the rGO-Fe_3O_4 3D frameworks with the aforementioned procedures for comparison, respectively.

2.3 Characterizations

The Fourier transform infrared spectroscopy (FTIR) of samples was carried out on a Thermo Nicolet NEXUS infrared spectrometer (Thermo Scientific Company, USA). Raman spectroscopy was analyzed by using an inVia micro-Raman spectrometer manufactured by Renishaw Company, UK. The X-ray diffraction (XRD) of samples was conducted on a D8 Advance X-ray powder diffractometer, Bruker Company, Germany. The samples were performed by X-ray photoelectron spectroscopy (XPS) using the AXIS Ultra DLD X-ray photoelectron spectrometer (Kratos Company, Japan). The morphology of samples was observed on an S-4800 scanning electron microscope (SEM, Hitachi Company, Japan). The transmission electron microscopy (TEM) images of samples were collected on a Tecnai G20, FEI Company, USA. The magnetic properties of samples at room temperature were studied by means of a vibrating sample magnetometer (VSM). The mechanical compression properties of samples were tested by a CTM1100 universal tensile testing machine (Shanghai Xieqiang Instruments and Equipment Co., Ltd.). The water contact angle of samples was measured by a JC2000 DS1 contact angle measuring instrument (Shanghai Zhongchen Digital Equipment Co., Ltd.). The nitrogen adsorption-desorption curves and pore size distributions curves of samples were measured on a TriStar 3020 specific surface area analyzer (Micromeritics Company).

2.4 Oil adsorption evaluation

The adsorption properties of samples were evaluated for oil and organic solvents including sesame oil, cyclohexane, ethyl acetate, acetone, and dichloromethane. The rGO-Fe_3O_4 3D frameworks were placed into a weighing bottle that contained the oil or organic solvent for adsorption. The adsorption process was holding for 5 min to make sure it reached an equilibrium. Actually, the adsorption process was very fast as the full removal of oil could be done within only several seconds. Therefore, the adsorption kinetics was not studied in this case. Then, the samples were taken out quickly to avoid the evaporation of oil or organic solvent. Finally, the weight of weighing bottles was recorded. The reduction of the weight

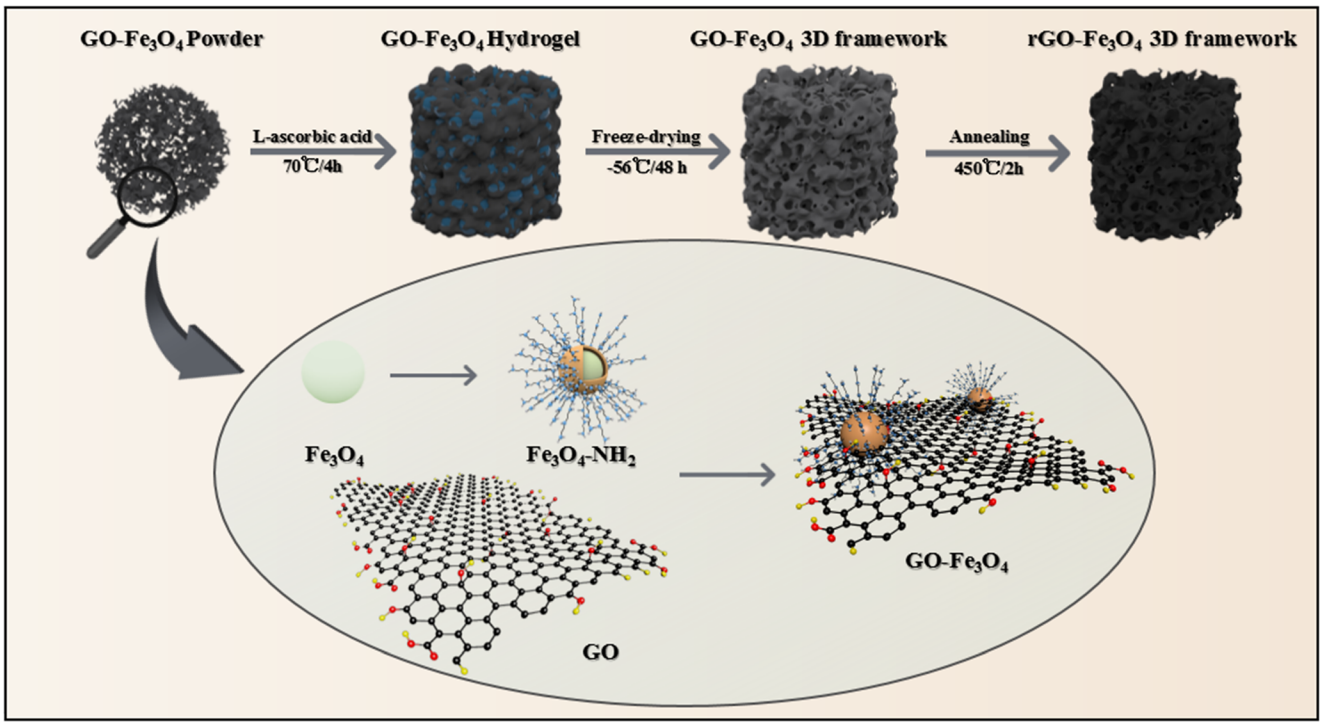

Fig. 1 Preparation procedures of rGO-Fe_3O_4 3D frameworks

for the weighing bottle was the adsorption capacity of the tested oil or organic solvent.

3 Results and discussion

3.1 Structure characterizations

Figure 2a shows the FT-IR spectra of Fe_3O_4-NH_2, GO, GO-Fe_3O_4 (before hydrothermal and annealing), and magnetic reduced graphene oxide (rGO-Fe_3O_4) 3D frameworks. The absorption peaks of GO at 1735, 1617, 1220, and 1047 cm^{-1} are the stretching vibration of C=O in the carboxyl group, C=C, C–O, and C–O–C, respectively, illustrating the formation of GO [32]. The stretching vibrations of the N–H bond and Fe–O bond at 1557 and 545 cm^{-1} in the FTIR spectrum of Fe_3O_4-NH_2 indicate the successful amination on the surface of Fe_3O_4 nanoparticles. Compared with GO, the stretching vibration of the C–N bond in the amide group of GO-Fe_3O_4 at 1405 cm^{-1} demonstrates that Fe_3O_4-NH_2 has been attached to the GO through a covalent bond between GO and Fe_3O_4-NH_2. For the rGO-Fe_3O_4 3D framework, the obvious disappearance of the C–O stretching vibrations at 1220 cm^{-1} and C–O–C at 1047 cm^{-1} indicates the reduction of GO in the rGO-Fe_3O_4 aerogel.

The Raman spectra of graphite, GO, reduced graphene oxide (rGO) aerogel, and the rGO-Fe_3O_4 3D framework are shown in Figure 2b. Compared with graphite, GO shows an increased D peak intensity (I_D) (D peak represents the structural defects) at 1350 cm^{-1} and a decreased G peak intensity (I_G) (G peak stands for the sp^2 C=C bond stretching vibrations) at 1580 cm^{-1} [33]. The ratio I_D/I_G increases from 0.13 for graphite to 1.36 for GO, suggesting the oxidation of graphite in the GO sample. After the chemical reduction by *L*-ascorbic acid and high-temperature annealing, I_D/I_G is decreased from 1.36 for GO to 1.33 for rGO aerogel and 1.27 for the rGO-Fe_3O_4 3D framework, indicating the restoration of the graphene defects [34].

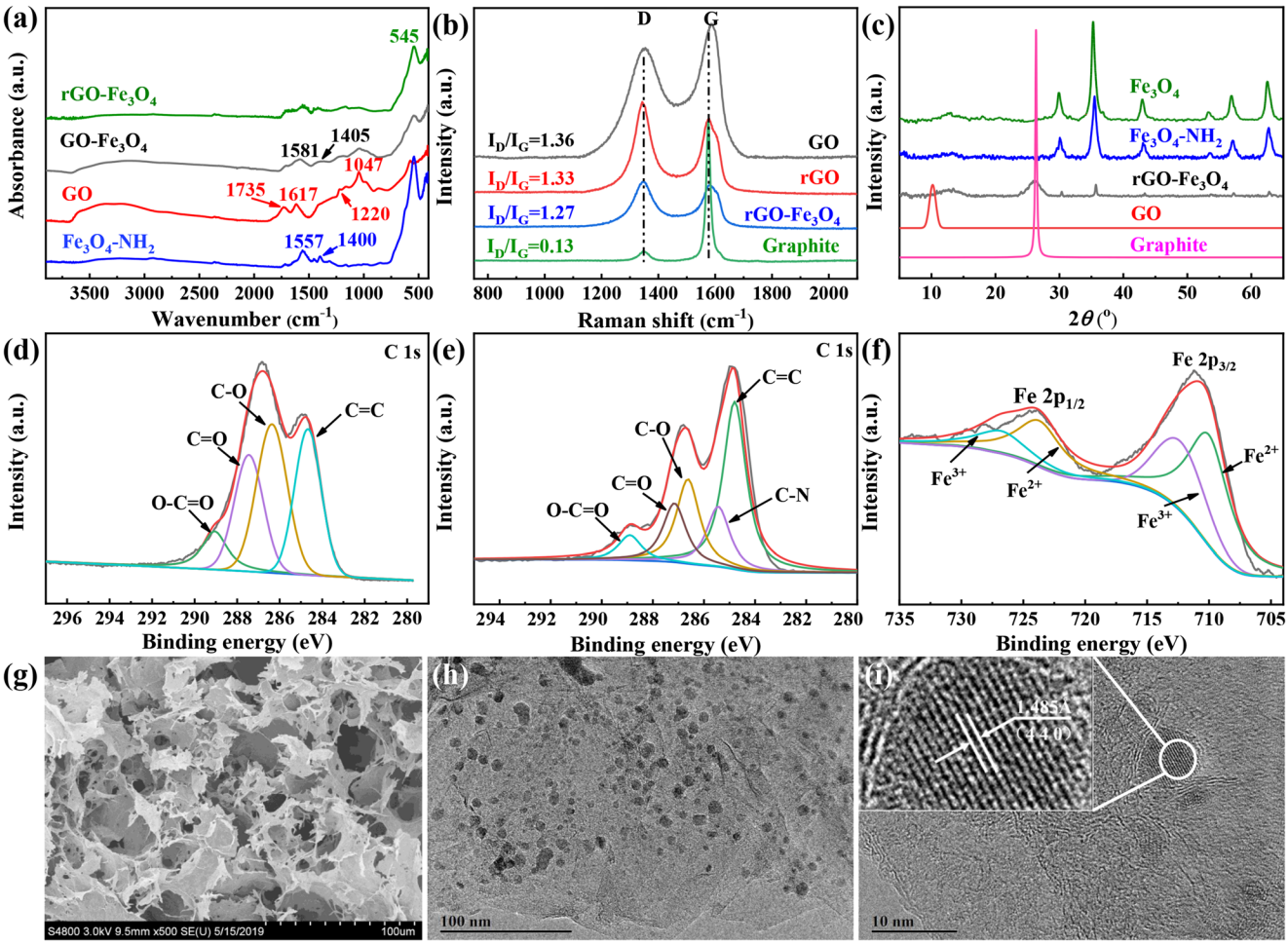

Fig. 2 **a** FTIR spectra of Fe_3O_4-NH_2, GO, GO-Fe_3O_4 (before annealing). and rGO-Fe_3O_4 aerogel. **b** Raman spectra of graphite, GO, rGO aerogel, and rGO-Fe_3O_4 aerogel. **c** XRD patterns of graphite, GO, rGO-Fe_3O_4 aerogel, and Fe_3O_4-NH_2. **d** High-resolution C 1s XPS spectra of GO. **e** High-resolution C 1s XPS spectra of rGO-Fe_3O_4 aerogel. **f** High-resolution Fe 2p XPS spectra of rGO-Fe_3O_4 aerogel. **g** SEM images of rGO-Fe_3O_4 aerogel. **h** TEM image and **i** high-resolution TEM image of rGO-Fe_3O_4 aerogel; inset shows the corresponding lattice fringe

Figure 2c depicts the XRD patterns of graphite, GO, Fe_3O_4-NH_2, and rGO-Fe_3O_4 3D framework. Graphite has a characteristic diffraction peak at $2\theta = 26.38°$, while that of GO is at $2\theta = 10.13°$. The change of the characteristic peak from graphite to GO is due to the increase of the interlayer distance coming from the intercalation of oxygen-containing functional groups into graphite sheets during the chemical oxidation process [35]. For the Fe_3O_4-NH_2 sample, the diffraction peaks at $2\theta = 18.02$, 29.87, 35.30, 36.81, 42.95, 53.38, 56.93, and 62.55° appear (Figure 2c), corresponding to the (1 1 1), (2 0 0), (3 1 1), (2 2 0), (4 0 0), (4 2 2), (5 1 1), and (4 4 0) crystallographic planes of Fe_3O_4 (PDF#65-3107) [36]. These characteristic diffraction peaks are also observed in the XRD pattern of the rGO-Fe_3O_4 3D framework. Moreover, the characteristic diffraction peak at $2\theta = 26.38°$ which is attributed to graphite appears in the XRD pattern of the rGO-Fe_3O_4 3D framework, illustrating the reduction of GO in the rGO-Fe_3O_4 3D framework.

The deconvoluted high-resolution C1s XPS spectra of GO (Figure 2d) shows four peaks at 284.6, 286.4, 287.5, and 289.1 eV, which are correlated with C=C, C-O, C=O, and O–C=O in the GO, respectively [37]. In comparison with GO, the characteristic peak of C–N at 285.4 eV in Figure 2e confirms the formation of the covalent bond between GO and Fe_3O_4-NH_2 in the rGO-Fe_3O_4 3D framework. The four peaks at 710.3 and 724.0, 712.9, and 727.0 eV (Figure 2f) in the rGO-Fe_3O_4 3D framework correspond to the $2p_{3/2}$, $2p_{1/2}$ signals of Fe^{2+} and the $2p_{3/2}$, $2p_{1/2}$ signals of Fe^{3+} in Fe_3O_4 nanoparticles [38].

Figure 2g gives the SEM image of the rGO-Fe_3O_4 3D framework, which exhibits a diverse micropore and 3D network microstructure. Figure 2h and i show the TEM images of the rGO-Fe_3O_4 3D framework at different magnifications. In Figure 2h, the Fe_3O_4 nanoparticles are uniformly distributed on the lamellar structure of graphene sheets, verifying the anchoring role of the covalent bond between Fe_3O_4-NH_2 and GO. The obvious lattice fringe in the high-resolution TEM (HRTEM) image of Figure 2i showing a lattice spacing of about 1.49 Å is assigned to the (4 4 0) crystallographic plane of Fe_3O_4, further implying the existence of Fe_3O_4 nanoparticles in the rGO-Fe_3O_4 3D framework.

3.2 Preparation conditions for optimum structure and adsorption performance of the rGO-Fe_3O_4 3D framework

In order to achieve the optimum structure and adsorption performance of rGO-Fe_3O_4, the preparation conditions include mass ratios of GO to Fe_3O_4-NH_2 and GO concentrations were discussed and a series of samples were synthesized for characterization. Firstly, the effect of preparation conditions on the microstructures of rGO-Fe_3O_4 3D framework was analyzed by SEM. Figure 3 depicts the SEM images of pure rGO aerogel and the rGO-Fe_3O_4 3D framework with different mass ratios of GO to Fe_3O_4-NH_2 including 4:1, 3:1, and 2:1. All these 3D frameworks have abundant pore structures with many wrinkles on the surface of graphene sheets. However, for the pure rGO aerogel (Figure 3a), the pore size is relatively smaller than that of rGO-Fe_3O_4 3D frameworks, Figure 3b-d. With the decrease in mass ratio of GO to Fe_3O_4-NH_2 (i.e., the increase of Fe_3O_4-NH_2 loading) from 4:1 to 2:1, the wrinkle of graphene lamellae gradually rises, and the pores in these 3D frameworks are obviously increased (Fig. 3b–d). Figure S1 depicts the SEM images of rGO-Fe_3O_4 3D frameworks prepared in different GO concentrations of 1, 2, 3, and 4 mg mL^{-1}. All these 3D frameworks have similarly big pores, which suggest that the large pore in the rGO-Fe_3O_4 3D framework is related not only to the GO concentrations but also to the mass ratio of GO to Fe_3O_4-NH_2, i.e., Fe_3O_4-NH_2 loadings. From the above results, it could be concluded that the Fe_3O_4-NH_2 nanoparticles are able to promote the linkage among different graphene lamellae to form the bigger pore structures. Abundant amino groups on the surface of Fe_3O_4-NH_2 could bond with the oxygen-containing groups on GO sheets through covalent bond, electrostatic force, and hydrogen bonding, which make the different GO sheets to be connected with each other. According to the above theory, a lower mass ratio of GO to Fe_3O_4-NH_2 would represent more interactions between Fe_3O_4-NH_2 and GO lamellae, resulting in the larger graphene lamellae and larger voids, as seen in the SEM results of Figure 3d. The possible formation mechanism of this rGO-Fe_3O_4 3D framework is present in Fig. 4.

Adsorption capacity is also a significant parameter to evaluate an absorbent like the rGO-Fe_3O_4 3D framework. Figure 5A and Figure S2 show the nitrogen adsorption-desorption curves and pore size distribution curves of rGO aerogel and rGO-Fe_3O_4 3D frameworks with different mass ratios of GO to Fe_3O_4-NH_2 and different GO concentrations, respectively. The nitrogen adsorption-desorption curves of all these aerogels display typical IV adsorption-desorption curves, signifying mesoporous characteristics [39]. The computed BET-specific surface area from nitrogen adsorption-desorption curves is 413.00, 88.04, 94.06, and 66.85 $m^2\ g^{-1}$ for rGO (Figure 5A (a)) and rGO-Fe_3O_4 3D frameworks with a GO to Fe_3O_4-NH_2 mass ratios of 4:1, 3:1, and 2:1 (Figure 5A (b–d)), respectively, illustrating that the addition of Fe_3O_4-NH_2 decreases the BET-specific surface area of rGO aerogel. Among rGO-Fe_3O_4 3D frameworks, the sample prepared with the GO to Fe_3O_4-NH_2 mass ratio of 3:1 possesses the highest BET-specific surface area. In addition, the BET-specific surface area of rGO-Fe_3O_4 3D frameworks with GO concentrations of 1, 2, 3, and 4 mg mL^{-1} is estimated to be 58.42, 87.32, 94.06, and 55.39 $m^2\ g^{-1}$, respectively (Figure S2-a, b, c, and d). The rGO-Fe_3O_4 3D framework prepared with a GO concentration of 3 mg mL^{-1} shows the highest BET-specific surface area. To further confirm the

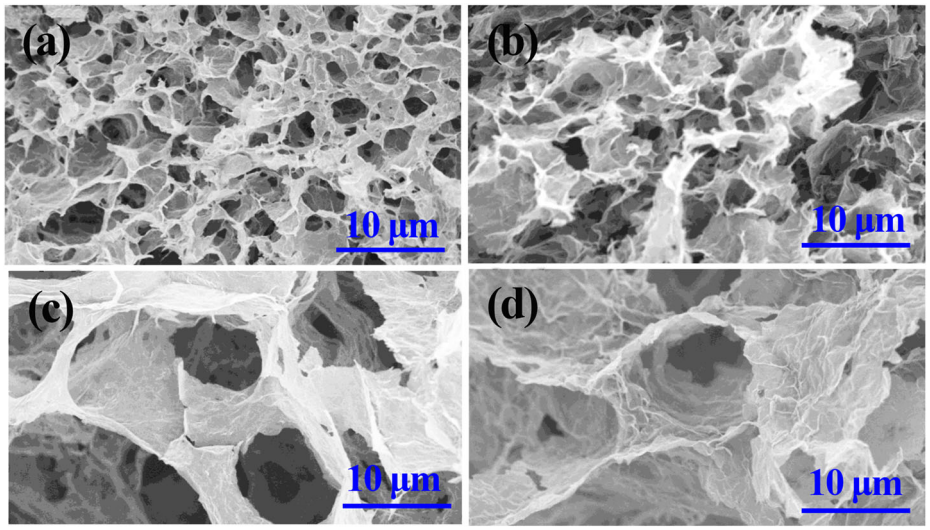

Fig. 3 SEM images of (**a**) rGO; rGO-Fe_3O_4 aerogel with GO to Fe_3O_4-NH_2 mass ratios of (**b**) 4:1; (**c**) 3:1; **d** 2:1

adsorption capacities of rGO-Fe_3O_4 3D frameworks, ethyl acetate adsorption tests were carried out for the samples fabricated with different mass ratios of GO to Fe_3O_4-NH_2 in different GO concentrations, shown in Figure 5B and Table S1. The ethyl acetate adsorption capacity is 215.8 ± 11.8, 108.1 ± 5.2, 86.0 ± 5.1, 86.6 ± 4.7, and 74.4 ± 3.4 g g^{-1} for the rGO-Fe_3O_4 aerogels produced under the GO concentrations of 1, 2, 3, 4, and 5 mg mL^{-1}, respectively, and 112.4 ± 6.1, 86.0 ± 5.1, and 50.3 ± 2.8 g g^{-1} for those produced in mass ratios of GO to Fe_3O_4-NH_2 of 2:1, 3:1, and 4:1, respectively. In contrast, the adsorption of ethyl acetate by rGO aerogel is only 45.6 ± 2.3 g g^{-1}. It is noted that the introduction of Fe_3O_4-NH_2 could significantly improve the adsorption capacity of ethyl acetate for rGO aerogel. In summary, although the BET-specific surface area of rGO-Fe_3O_4 3D frameworks is relatively lower than that of rGO aerogel, the organic solvent adsorption capacity of rGO-Fe_3O_4 3D frameworks is much higher than that of rGO aerogel.

By considering the BET results, SEM results, and the ethyl acetate adsorption results, the relationship between microstructures and adsorption capacities of rGO-Fe_3O_4 3D frameworks could also be figured out. The higher

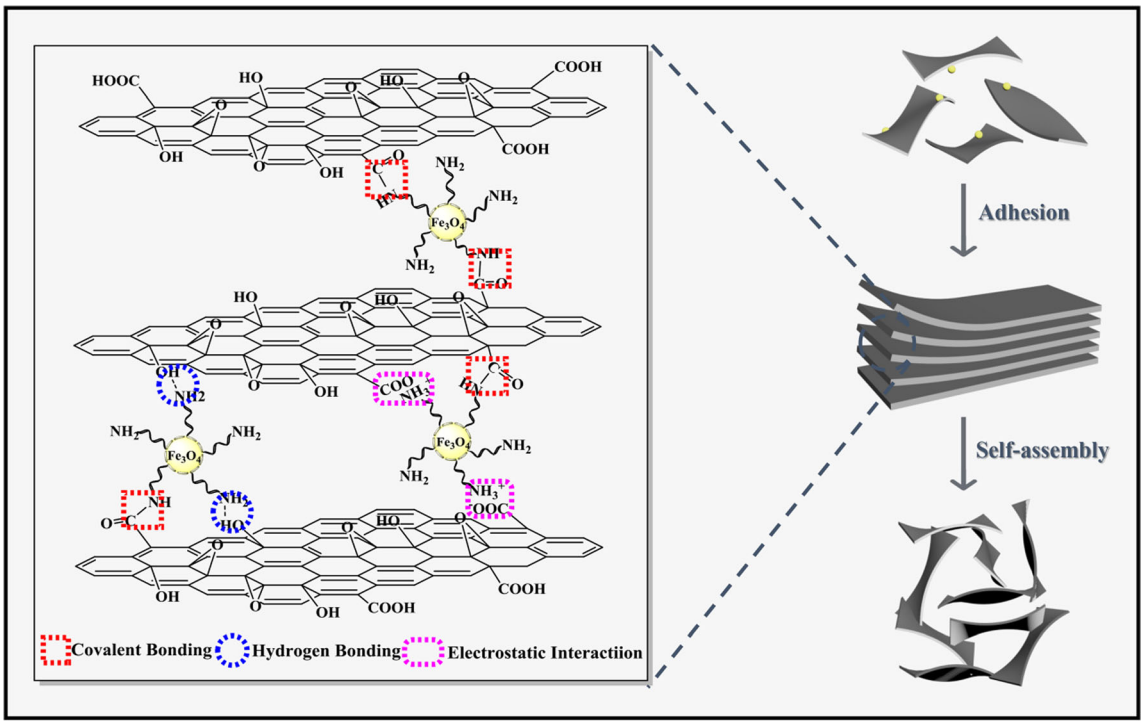

Fig. 4 Proposed principle of the formation mechanism of rGO-Fe_3O_4 aerogel, in which graphene lamellar connection is induced by Fe_3O_4-NH_2

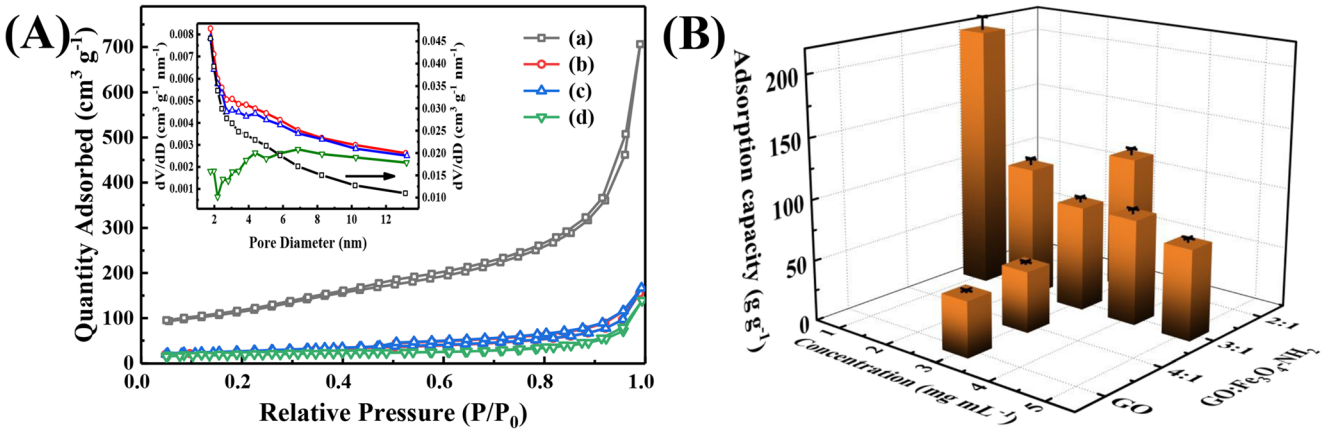

Fig. 5 A Nitrogen adsorption-desorption curves and pore size distribution curves of **a** rGO aerogel and rGO-Fe_3O_4 3D framework with GO to Fe_3O_4-NH_2 mass ratios of (b) 2:1, (c) 3:1, and (d) 4:1. **B** Adsorption capacity of rGO-Fe_3O_4 3D framework with different GO concentrations and GO to Fe_3O_4-NH_2 mass ratios on ethyl acetate

organic solvent adsorption capability of rGO-Fe_3O_4 3D frameworks might be from their larger pore structures. On the one hand, this larger macroscopic porous structure in rGO-Fe_3O_4 3D frameworks provides the capillarity [40], and the capillary effect of pores plays an important role during the oil adsorption process. On the other hand, the larger pore structure is also capable of promoting the oil and organic solvent transportation within the networks, leading to a higher adsorption performance. As a consequence, the adsorption capacity of rGO-Fe_3O_4 3D frameworks is remarkably enhanced.

To determine the optimal preparation conditions of rGO-Fe_3O_4 3D frameworks, their mechanical properties must also be considered. For example, although the adsorption capacity of ethyl acetate by the rGO-Fe_3O_4 3D frameworks fabricated with a GO to Fe_3O_4-NH_2 mass ratio of 2:1 (112.4 g g^{-1}) is higher than that of 3:1 (86.0 g g^{-1}), the mechanical strength of the rGO-Fe_3O_4 3D framework fabricated with a GO to Fe_3O_4-NH_2 mass ratio of 2:1 is not that good as that of 3:1, i.e., the rGO-Fe_3O_4 3D framework fabricated with a GO to Fe_3O_4-NH_2 mass ratio of 2:1 is relatively easier to be broken. Similarly, the rGO-Fe_3O_4 3D framework synthesized with high GO concentrations (like 5 mg L^{-1}) is very fragile (i.e., easy to de destroyed, supplementary video S1 and its elasticity is very poor, unlike the rGO-Fe_3O_4 3D framework fabricated with a GO concentration of 1 mg mL^{-1} that exhibits excellent elasticity (supplementary video S2). The poor mechanical property is not beneficial to the reusability of the rGO-Fe_3O_4 3D framework. Hence, taking into account the microstructures, adsorption ability, mechanical property, and reusability, the optimal preparation conditions of rGO-Fe_3O_4 aerogels are recognized as the mass ratio of GO to Fe_3O_4-NH_2 of 3:1 in the 1 mg mL^{-1} of the GO concentration.

3.3 Mechanical properties and adsorption performance of the rGO-Fe_3O_4 3D framework

The left side of Figure 6A provides a close-up photograph of the rGO-Fe_3O_4 3D framework that is able to be maintained on the stamen of a flower. Its density is evaluated to be 4.52 mg cm^{-3} through measuring its height and diameter as displayed on the right side of Figure 6A, suggesting that our rGO-Fe_3O_4 3D framework is ultra-light (which means that the density of material is less than 10 mg cm^{-3}). The water contact angle of the rGO-Fe_3O_4 3D framework as demonstrated in the left inset of Figure 6A is 134.99°, representing a superhydrophobic characteristic of the rGO-Fe_3O_4 3D framework. With the superhydrophobic and lipophilic properties, the rGO-Fe_3O_4 3D framework would have great application prospects in offshore oil spill and organic solvent waste treatment [41], since the superhydrophobic property facilitates the material to adsorb the grease [42].

The mechanical property of the rGO-Fe_3O_4 3D framework is studied via the compression test. As revealed in the inset of Figure 6B, the compression strain-stress curve under the condition of 80% compression strain, the rGO-Fe_3O_4 3D framework discloses an excellent stability and resilience with a 100% recovery, the photographs in the insert of Figure 6B. The compression stress-strain curves of the rGO-Fe_3O_4 3D framework during the 10 cycles of the compression process under the 40% deformation of the strain is displayed in Fig. 6B (For the purpose of 100% recovery and reusability of the rGO-Fe_3O_4 3D framework within the cyclic test, 40% deformation of stain was chosen.) After 10 cycles of deformation, the rGO-Fe_3O_4 3D framework could completely revert to its original state and maintain almost the same compression performance, showing an excellent structural strength and a repeatable compression cycle capability. This stable superelastic

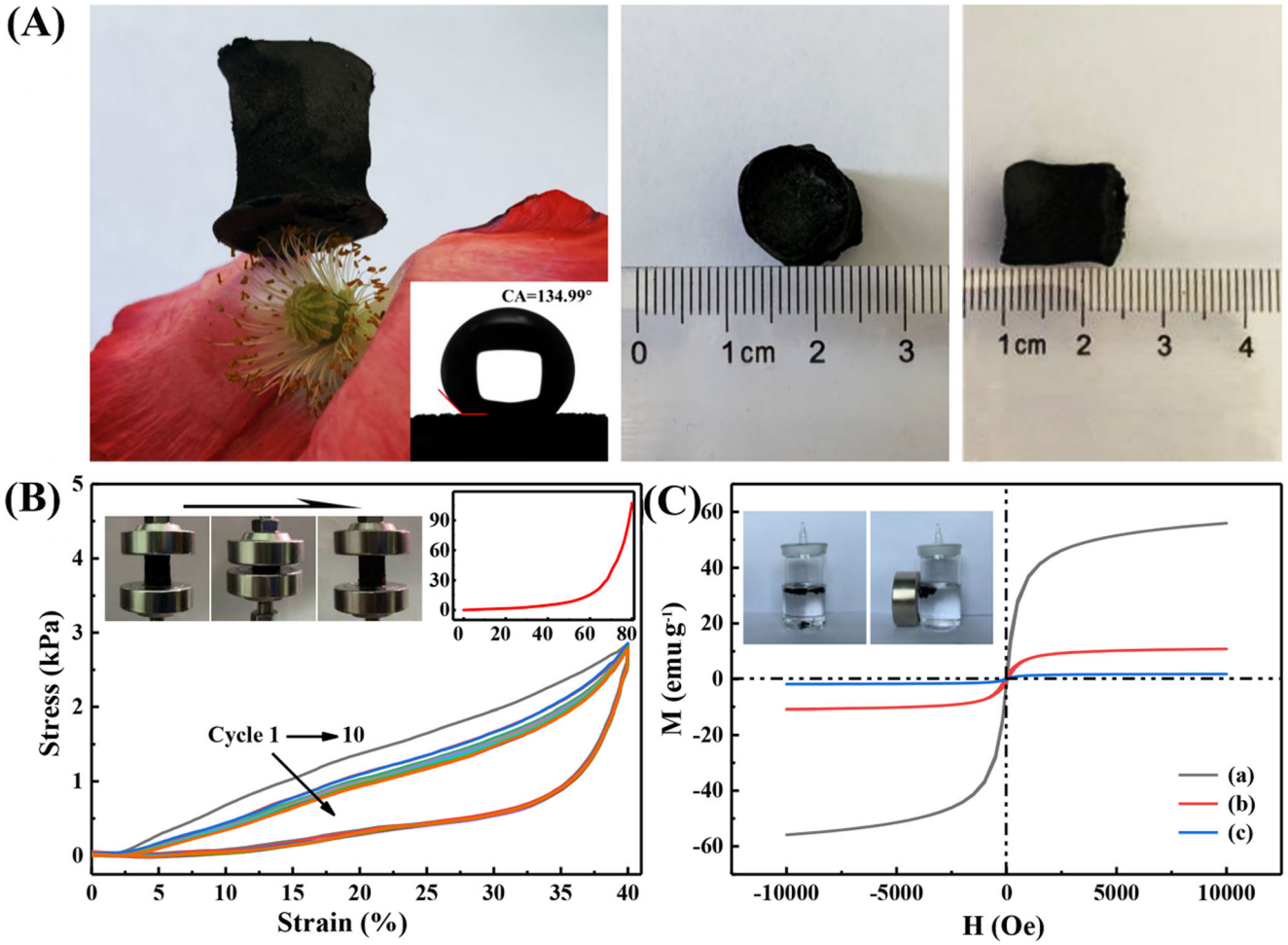

Fig. 6 **A** Digital photographs of the rGO-Fe_3O_4 3D framework placed on a flower, diameter, and height measurements; inset of left photographs indicates the water contact angle of the rGO-Fe_3O_4 3D framework. **B** Eighty percent strain compression test and compression cycle tests under 40% strain of the rGO-Fe_3O_4 3D framework. **C** Magnetization curves of (a) Fe_3O_4 and (b) rGO-Fe_3O_4 3D framework with GO to Fe_3O_4-NH_2 mass ratios of 2:1 and 3:1 at room temperature

structure provides a great possibility and operability for the reuse of our rGO-Fe_3O_4 3D framework after the adsorption of oil and organic solvents.

Figure 6C gives the magnetization curves of Fe_3O_4 and the rGO-Fe_3O_4 3D framework prepared with a GO to Fe_3O_4-NH_2 mass ratio of 2:1 and 3:1 at room temperature. Compared with pure Fe_3O_4 nanoparticles, the saturation magnetization of the rGO-Fe_3O_4 3D framework with a GO to Fe_3O_4-NH_2 mass ratio of 2:1 and 3:1 is decreased from 55.9 (for pure Fe_3O_4 nanoparticles) to 10.8 and 1.8 emu g^{-1}, respectively. The rGO-Fe_3O_4 3D framework could still be adsorbed by a permanent magnet after adsorbing ethyl acetate, whose weight is 215.8 times higher than the 3D framework itself (photographs in Figure 6C), expressing a good magnetic property of the rGO-Fe_3O_4 3D framework. This supplies the convenience for recycling the rGO-Fe_3O_4 3D framework after adsorption during the practical application.

After dying cyclohexane with Sudan Red B, the oil/water separation experiments by the rGO-Fe_3O_4 3D framework have been carried out, as shown in Figure 7a. It is observed that the hyperelastic rGO-Fe_3O_4 3D framework is capable of efficiently adsorbing cyclohexane from the water surface and achieving an extraction of cyclohexane from water within only 25 s. This rapid oil/water separation ability offers the possibility and convenience for large-scale oil spill and organic solvent waste removal from water.

The adsorption capacities of the superelastic rGO-Fe_3O_4 3D framework are evaluated by selecting ethyl acetate, cyclohexane, dichloromethane, sesame oil, and acetone as representative oil and organic solvents, and the results are revealed in Figure 7b. The rGO-Fe_3O_4 3D framework displays an outstanding adsorption capacity for all kinds of oil and organic solvents, for example, ethyl acetate (215.8 ± 11.8 g g^{-1}), cyclohexane (239.7 ± 9.9 g g^{-1}), acetone (149.1 ± 6.5 g g^{-1}), dichloromethane (308.0 ± 16.4 g g^{-1}), and sesame oil (204.7 ± 10.2 g g^{-1}). Table 1 shows the comparison chart of the adsorption capacity for different graphene aerogel materials reported in literature for oil and organic solvent treatment, as

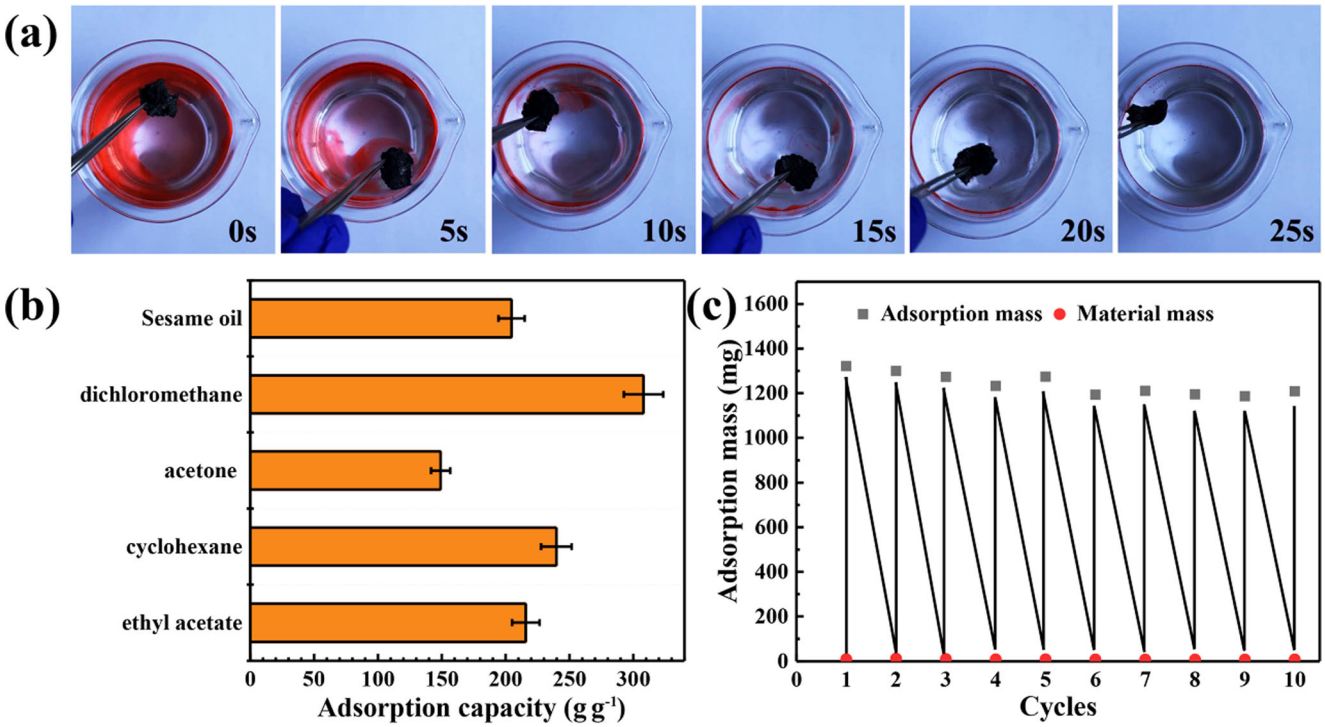

Fig. 7 **a** Digital photos depict the oil-water separation tests of the rGO-Fe_3O_4 3D framework. **b** Adsorption capacity of the rGO-Fe_3O_4 3D framework for different oil and organic solvents. **c** Cyclic adsorption experiments of ethyl acetate adsorption by the rGO-Fe_3O_4 3D framework

Table 1 Comparison of properties for different graphene aerogels in literature

Materials	Density (mg cm^{-3})	Compressibility	Magnetic property	Adsorption capacity (g g^{-1})
Graphene/carbon nanotube aerogel [43]	3.0	Compressible	Non-magnetic	*n*-Hexane 180 Chloroform 140 Vegetable oil 170
Modified cellulose/graphene aerogel [44]	5.9	Compressible	Non-magnetic	Hexane 80 Chloroform 190
3D graphene/iron oxide aerogel [45]	5.8	Compressible	Strong magnetic	Gasoline 150
Nitrogen-doped graphene framework [46]	2.1	Incompressible	Non-magnetic	Acetone 340 Cyclohexane 330
Graphene/MWCNT-PDA composite aerogel [47]	2.1	Compressible	Non-magnetic	*n*-Hexane 250 Acetone 200
Graphene aerogel [48]	6.0	Compressible	Non-magnetic	*n*-Hexane 125 Dichloromethane 200
Anisotropic graphene aerogel [49]	4.2	Compressible	Non-magnetic	*n*-Hexane 135 Acetone 160
Magnetic graphene/CNT foam [24]	2.1	Incompressible	Magnetic	Hexane 15 Chloroform 20
Reduced graphene oxide foam [50]	8.0	Compressible	Non-magnetic	Chloroform: 100
Magnetic reduced graphene oxide 3D framework[a]	*4.52*	*Compressible*	*Magnetic*	*Ethyl estate 215.8* *Cyclohexane 239.7* *Dichloromethane 308.0* *Acetone 149.1* *Sesame oil 204.7*

[a] Results obtained in this work.

well as their density, elasticity, and magnetic properties. It is figured out that our rGO-Fe_3O_4 3D framework owns a low-density (4.52 mg cm^{-3}), high-resilience, and excellent magnetic property that boosts the recovery, regeneration, and reuse of materials, as well as high adsorption capacity for various organic pollutants and oil products.

The reusability of the rGO-Fe_3O_4 3D framework is also taken into account. In this work, 10-cycle adsorption-desorption experiments of ethyl acetate were carried out by using this superelastic rGO-Fe_3O_4 3D framework (Figure 7c). Owing to the high elasticity of the rGO-Fe_3O_4 3D framework, we have removed part of ethyl acetate by compressing the 3D framework after adsorption and then used the volatilization characteristics of ethyl acetate to quickly eliminate the residual ethyl acetate in the 3D framework. The weight and structure as well as adsorption properties of rGO-Fe_3O_4 3D framework after removing ethyl acetate have no obvious change. After 10 cycles of adsorption-desorption processes, the adsorption capacity of the rGO-Fe_3O_4 3D framework is almost the same as that at the beginning (Figure 7c). As a result, our rGO-Fe_3O_4 3D framework has very superb reusability for practical applications. Unfortunately, our rGO-Fe_3O_4 3D framework has no obvious flammability, so we could not use the burning method to remove the oil from the 3D framework since the oil could not be volatilized. Therefore, we have only done the volatile ethyl acetate for the reusability tests.

4 Conclusions

To sum up, an efficient recyclable and reusable superelastic magnetic rGO-Fe_3O_4 3D framework has been developed by the covalent bond of Fe_3O_4-NH_2 on GO with a further reduction process. The covalent bond between Fe_3O_4-NH_2 and GO could help Fe_3O_4 nanoparticles to be uniformly distributed within graphene sheets as verified in HRTEM images, and the reduction process could increase the hydrophobic property of the 3D framework that is beneficial for its oil and organic solvent adsorption. The optimal condition for preparing a high-performance rGO-Fe_3O_4 3D framework is the 1 mg mL^{-1} concentration of GO, and a 3:1 mass ratio of GO to Fe_3O_4-NH_2. The adsorption capacity of this superelastic rGO-Fe_3O_4 aerogel for ethyl acetate, cyclohexane, acetone, dichloromethane, and sesame oil is 215.8 ± 11.8, 239.7 ± 9.9, 149.1 ± 6.5, 308.0 ± 16.4, and 204.7 ± 10.2 g g^{-1}, evincing a superior adsorption capacity and oil/water separation ability compared with the reported results in the literature. In addition, our rGO-Fe_3O_4 3D framework holds a very low density (4.52 mg cm^{-3}), prominent elasticity, and good magnetic properties, ensuring its recoverability and reusability in practical applications. Hence, this magnetic rGO-Fe_3O_4 3D framework is expected to be used as a prospective adsorption material for oil and organic solvent pollution control and treatment.

Supplementary Information The online version contains supplementary material available at https://doi.org/10.1007/s42114-020-00191-z.

Funding The authors were financially supported by the Foundation of National Natural Science Foundation of China (No. 51703165), Shanghai Rising-Star Program (No. 19QA1409400), and Science and Technology Commission of Shanghai Municipality (19DZ2271500).

Compliance with ethical standards

Conflict of interest The authors declare that they have no conflict of interest.

References

1. Ge J, Shi LA, Wang YC, Zhao HY, Yao HB, Zhu YB, Zhang Y, Zhu HW, Wu HA, Yu SH (2017) Joule-heated graphene-wrapped sponge enables fast clean-up of viscous crude-oil spill. Nat Nanotechnol 12:434
2. Perrons RK (2013) Assessing the damage caused by Deepwater Horizon: not just another Exxon Valdez. Mar Pollut Bull 71(1): 20–22
3. Schrope M (2011) Oil spill: deep wounds. Nature 472(7342):152–154
4. Zhou X, Fu Q, Liu H, Gu H, Guo Z (2021) Solvent-free nanoalumina loaded nanocellulose aerogel for efficient oil and organic solvent adsorption. J Colloid Interface Sci 581: 299-306
5. Zhang H, Lyu S, Zhou X, Gu H, Ma C, Wang C, Ding T, Shao Q, Liu H, Guo Z (2019) Super light 3D hierarchical nanocellulose aerogel foam with superior oil adsorption. J Colloid Interface Sci 536:245–251
6. Ge J, Wang F, Yin X, Yu J, Ding B (2018) Polybenzoxazine-functionalized melamine sponges with enhanced selective capillarity for efficient oil spill cleanup. ACS Appl Mater Interfaces 10(46): 40274–40285
7. Wu M, Shi Y, Chang J, Li R, Ong C, Wang P (2018) Sunlight induced rapid oil absorption and passive room-temperature release: an effective solution toward heavy oil spill cleanup. Adv Mater Interfaces 5(14):1800412
8. Yang X, Wang Z, Shao L (2018) Construction of oil-unidirectional membrane for integrated oil collection with lossless transportation and oil-in-water emulsion purification. J Membr Sci 549:67–74
9. Sun H, Zhang Y, Sadam H, Ma J, Bai Y, Shen X, Kim JK, Shao L (2019) Novel mussel-inspired zwitterionic hydrophilic polymer to boost membrane water-treatment performance. J Membr Sci 582:1–8
10. Sun H, Yang X, Zhang Y, Cheng X, Xu Y, Bai Y, Shao L (2018) Segregation-induced in situ hydrophilic modification of poly (vinylidene fluoride) ultrafiltration membranes via sticky poly (ethylene glycol) blending. J Membr Sci 563:22–30
11. Jaggi A, Radović JR, Snowdon LR, Larter SR, Oldenburg TBP (2019) Composition of the dissolved organic matter produced during in situ burning of spilled oil. Org Geochem 138:103926
12. Zhang X, Wang X, Liu X, Lv C, Wang Y, Zheng G, Liu H, Liu C, Guo Z, Shen C (2018) Porous polyethylene bundles with enhanced hydrophobicity and pumping oil-recovery ability via skin-peeling. ACS Sustain Chem Eng 6(10):12580–12585

13. Song S, Yang H, Su C, Jiang Z, Lu Z (2016) Ultrasonic-microwave assisted synthesis of stable reduced graphene oxide modified melamine foam with superhydrophobicity and high oil adsorption capacities. Chem Eng J 306:504–511
14. Wu MN, Maity JP, Bundschuh J, Li CF, Lee CR, Hsu CM, Lee WC, Huang CH, Chen CY (2017) Green technological approach to synthesis hydrophobic stable crystalline calcite particles with one-pot synthesis for oil-water separation during oil spill cleanup. Water Res 123:332–344
15. Kazemzadeh Y, Eshraghi SE, Kazemi K, Sourani S, Mehrabi M, Ahmadi Y (2015) Behavior of asphaltene adsorption onto the metal oxide nanoparticle surface and its effect on heavy oil recovery. Ind Eng Chem Res 54(1):233–239
16. Shayan NN, Mirzayi B (2015) Adsorption and removal of asphaltene using synthesized maghemite and hematite nanoparticles. Energy Fuel 29(3):1397–1406
17. Kayvani Fard A, Rhadfi T, McKay G, Al-marri M, Abdala A, Hilal N, Hussien MA (2016) Enhancing oil removal from water using ferric oxide nanoparticles doped carbon nanotubes adsorbents. Chem Eng J 293:90–101
18. Štefelová J, Slovák V, Siqueira G, Olsson RT, Tingaut P, Zimmermann T, Sehaqui H (2017) Drying and pyrolysis of cellulose nanofibers from wood, bacteria, and algae for char application in oil absorption and dye adsorption. ACS Sustain Chem Eng 5(3): 2679–2692
19. Wang X, Yu J, Sun G, Ding B (2016) Electrospun nanofibrous materials: a versatile medium for effective oil/water separation. Mater Today 19(7):403–414
20. Zhou X, Zhang Z, Xu X, Guo F, Zhu X, Men X, Ge B (2013) Robust and durable superhydrophobic cotton fabrics for oil/water separation. ACS Appl Mater Interfaces 5(15):7208–7214
21. Cheng QY, Guan CS, Li YD, Zhu J, Zeng JB (2019) Robust and durable superhydrophobic cotton fabrics via a one-step solvothermal method for efficient oil/water separation. Cellulose 26(4):2861–2872
22. Yue X, Li J, Zhang T, Qiu F, Yang D, Xue M (2017) In situ one-step fabrication of durable superhydrophobic-superoleophilic cellulose/LDH membrane with hierarchical structure for efficiency oil/water separation. Chem Eng J 328:117–123
23. Sun H, Xu Z, Gao C (2013) Multifunctional, ultra-flyweight, synergistically assembled carbon aerogels. Adv Mater 25(18):2554–2560
24. Yang S, Chen L, Mu L, Ma PC (2014) Magnetic graphene foam for efficient adsorption of oil and organic solvents. J Colloid Interface Sci 430:337–344
25. Zhou S, Jiang W, Wang T, Lu Y (2015) Highly hydrophobic, compressible, and magnetic polystyrene/Fe_3O_4/graphene aerogel composite for oil-water separation. Ind Eng Chem Res 54(20):5460–5467
26. Kuila T, Bose S, Mishra AK, Khanra P, Kim NH, Lee JH (2012) Chemical functionalization of graphene and its applications. Prog Mater Sci 57(7):1061–1105
27. Tuček J, Kemp KC, Kim KS, Zbořil R (2014) Iron-oxide-supported nanocarbon in lithium-ion batteries, medical, catalytic, and environmental applications. ACS Nano 8(8):7571–7612
28. Liang C, Song P, Ma A, Shi X, Gu H, Wang L, Qiu H, Kong J, Gu J (2019) Highly oriented three-dimensional structures of Fe_3O_4 decorated CNTs/reduced graphene oxide foam/epoxy nanocomposites against electromagnetic pollution. Compos Sci Technol 181: 107683
29. Gao F, Gu H, Wang H, Wang X, Xiang B, Guo Z (2015) Magnetic amine-functionalized polyacrylic acid-nanomagnetite for hexavalent chromium removal from polluted water. RSC Adv 5(74):60208–60219
30. Cai J, Tian J, Gu H, Guo Z (2019) Amino carbon nanotube modified reduced graphene oxide aerogel for oil/water separation. ES Mater Manuf 6:68–74
31. Gao J, Liu F, Liu Y, Ma N, Wang Z, Zhang X (2010) Environment-friendly method to produce graphene that employs vitamin C and amino acid. Chem Mater 22(7):2213–2218
32. Chang X, Wang Z, Quan S, Xu Y, Jiang Z, Shao L (2014) Exploring the synergetic effects of graphene oxide (GO) and polyvinylpyrrodione (PVP) on poly(vinylylidenefluoride) (PVDF) ultrafiltration membrane performance. Appl Surf Sci 316:537–548
33. Gu H, Xu X, Dong M, Xie P, Shao Q, Fan R, Liu C, Wu S, Wei R, Guo Z (2019) Carbon nanospheres induced high negative permittivity in nanosilver-polydopamine metacomposites. Carbon 147: 550–558
34. Song P, Liang C, Wang L, Qiu H, Gu H, Kong J, Gu J (2019) Obviously improved electromagnetic interference shielding performances for epoxy composites via constructing honeycomb structural reduced graphene oxide. Compos Sci Technol 181:107698
35. Feng J, Li F, Li X, Ren X, Fan D, Wu D, Ma H, Du B, Zhang N, Wei Q (2019) An amplification label of core-shell CdSe@CdS QD sensitized GO for a signal-on photoelectrochemical immunosensor for amyloid β-protein. J Mater Chem B 7(7):1142–1148
36. Gu H, Zhou X, Lyu S, Pan D, Dong M, Wu S, Ding T, Wei X, Seok I, Wei S, Guo Z (2020) Magnetic nanocellulose-magnetite aerogel for easy oil adsorption. J Colloid Interface Sci 560:849–856
37. Lou C, Jing T, Tian J, Zheng Y, Zhang J, Dong M, Wang C, Hou C, Fan J, Guo Z (2019) 3-Dimensional graphene/Cu/Fe_3O_4 composites: immobilized laccase electrodes for detecting bisphenol A. J Mater Res 34(17):2964–2975
38. Gu H, Lou H, Tian J, Liu S, Tang Y (2016) Reproducible magnetic carbon nanocomposites derived from polystyrene with superior tetrabromobisphenol A adsorption performance. J Mater Chem A 4(26):10174–10185
39. Huang C, Shi X, Wang C, Guo L, Dong M, Hu G, Lin J, Ding T, Guo Z (2019) Boosted selectivity and enhanced capacity of As(V) removal from polluted water by triethylenetetramine activated lignin-based adsorbents. Int J Biol Macromol 140:1167–1174
40. Fu Y, Wang G, Mei T, Li J, Wang J, Wang X (2017) Accessible graphene aerogel for efficiently harvesting solar energy. ACS Sustain Chem Eng 5(6):4665–4671
41. Liu L, Pan Y, Bhushan B, Zhao X (2019) Mechanochemical robust, magnetic-driven, superhydrophobic 3D porous materials for contaminated oil recovery. J Colloid Interface Sci 538:25–33
42. Wang Y, Wang B, Wang J, Ren Y, Xuan C, Liu C, Shen C (2018) Superhydrophobic and superoleophilic porous reduced graphene oxide/polycarbonate monoliths for high-efficiency oil/water separation. J Colloid Interface Sci 344:849–856
43. Zhao D, Yu L, Liu D (2018) Ultralight graphene/carbon nanotubes aerogels with compressibility and oil absorption properties. Materials 11(4):641
44. Mi HY, Jing X, Politowicz AL, Chen E, Huang HX, Turng LS (2018) Highly compressible ultra-light anisotropic cellulose/graphene aerogel fabricated by bidirectional freeze drying for selective oil absorption. Carbon 132:199–209
45. Xu X, Li H, Zhang Q, Hu H, Zhao Z, Li J, Li J, Qiao Y, Gogotsi Y (2015) Self-sensing, ultralight, and conductive 3D graphene/iron oxide aerogel elastomer deformable in a magnetic field. ACS Nano 9(4):3969–3977
46. Zhao Y, Hu C, Hu Y, Cheng H, Shi G, Qu L (2012) A versatile, ultralight, nitrogen-doped graphene framework. Angew Chem Int Ed 51(45):11371–11375
47. Zhan W, Yu S, Gao L, Wang F, Fu X, Sui G, Yang X (2018) Bioinspired assembly of carbon nanotube into graphene aerogel with "cabbagelike" hierarchical porous structure for highly efficient organic pollutants cleanup. ACS Appl Mater Interfaces 10(1): 1093–1103

48. Li J, Li J, Meng H, Xie S, Zhang B, Li L, Ma H, Zhang J, Yu M (2014) Ultra-light, compressible and fire-resistant graphene aerogel as a highly efficient and recyclable absorbent for organic liquids. J Mater Chem A 2(9):2934–2941
49. Liu T, Huang M, Li X, Wang C, Gui CX, Yu ZZ (2016) Highly compressible anisotropic graphene aerogels fabricated by directional freezing for efficient absorption of organic liquids. Carbon 100: 456–464
50. He Y, Liu Y, Wu T, Ma J, Wang X, Gong Q, Kong W, Xing F, Liu Y, Gao J (2013) An environmentally friendly method for the fabrication of reduced graphene oxide foam with a super oil absorption capacity. J Hazard Mater 260:796–805